PHYSICAL REVIEW B VOLUME 50, NUMBER 8 15 AUGUST 1994-II

Exciton dimensionality and confinement studied by resonant Raman scattering in GaAs/Al$_x$Ga$_{1-x}$As Bragg-confining structures and superlattices

M. Zahler, E. Cohen, J. Salzman, E. Linder, and E. Maayan
Solid State Institute, Technion-Israel Institute of Technology, Haifa 32000, Israel

L. N. Pfeiffer
AT&T Bell Laboratories, Murray Hill, New Jersey 07974

(Received 17 March 1994)

The LO-phonon resonant Raman scattering is studied in GaAs/Al$_{0.32}$Ga$_{0.68}$As Bragg-confining structures at low temperatures. Comparative studies are made on a GaAs/Al$_{0.32}$Ga$_{0.68}$As superlattice and on a bulk Al$_{0.3}$Ga$_{0.7}$As crystal. A strong scattering intensity is observed in the spectral range of the $(e_B\text{:hh}_B)1S$, $(e_B\text{:lh}_B)1S$ Bragg-confined excitons and the $(e_1\text{:hh}_1)1S$ superlattice exciton. The Raman profiles, namely, the scattering intensity versus exciting laser energy (in the respective spectral ranges) are characterized by a large outgoing-beam/incoming-beam intensity ratio. These profiles are analyzed in terms of a model based on exciton confinement, on the anisotropy of its $1S$ wave function (which defines its dimensionality), and on its scattering by interface and alloy potential fluctuations. The $(e_B\text{:hh}_B)1S$ exciton is thus found to be virtually two-dimensional, while the $(e_B\text{:lh}_B)1S$ and $(e_1\text{:hh}_1)1S$ excitons are intermediate between two and three dimensions. The dimensionality is found to be related to the degree of confinement.

I. INTRODUCTION

In a Bragg-confining structure (BCS),[1-4] the confinement mechanism is based on two requirements. (a) The carrier wave function must be coherent over a long distance (in the confinement direction; that is, in the growth direction z). (b) The carrier de Broglie wavelength along the confinement direction must fulfill a Bragg reflection condition, so that its wave-function amplitude outside the barriers is greatly reduced. In such a BCS, properly designed superlattice (SL) sections act as Bragg reflectors for an electron and a hole confined in the barrier. This results in a discrete energy level (for each particle), that falls within the first SL mini stop band; that is, the energy gap between the first two subbands. These are termed Bragg-confined (BC) states. The BCS unit cell and the calculated energy subbands of electrons, heavy holes, and light holes are schematically shown in Fig. 1. The corresponding BC states are denoted e_B, hh$_B$, and lh$_B$, respectively. In undoped BCS's, the excitons made of the confined carriers, $(e_B\text{:hh}_B)$ and $(e_B\text{:lh}_B)$, have been observed by the photoluminescence (PL), its excitation (PLE) spectra,[1] and by LO-phonon resonant Raman scattering (RRS).[4,5] Transitions between the lowest electron and hole Landau levels were observed in BCS's under an applied magnetic field.[6] In n-doped BCS's, an intersubband transition between the well-confined to Bragg-confined electron states has been observed.[2,3,7]

We present a study of the low-temperature LO-phonon RRS, in three undoped GaAs/Al$_{0.32}$Ga$_{0.68}$As structures: two BCS's (with different degrees of Bragg confinement), an ordinary SL having the same period as the Bragg reflectors in both BCS's, and a bulk Al$_{0.3}$Ga$_{0.7}$As crystal. A comparison between the LO-phonon RRS profiles, namely the scattering intensity dependence on the excitations (laser) energy, allows us to examine in detail the excitonic properties that affect the RRS. Such profiles were previously studied in quantum wells (QW's) and SL's,[8-13] and were analyzed in terms of models that assume excitons to be the intermediate states in the RRS. Various mechanisms were proposed in order to explain the strong scattering intensity, the asymmetry between the incoming beam (IB) and outgoing beam (OB) resonances, and the spectral shape (inhomogeneous broadening). The mecha-

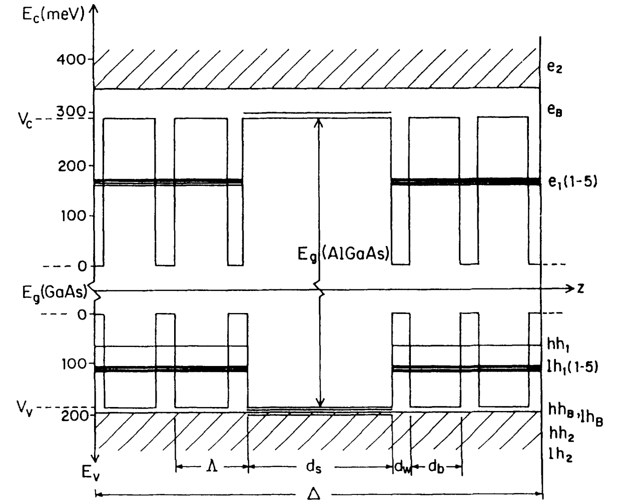

FIG. 1. A schematic description of the Bragg-confining structure "unit cell" and energy subbands. The band offset ratio is taken as 60/40.

0163-1829/94/50(8)/5305(11)/$06.00

nisms were based on the subband structure and on breaking the in-plane wave-vector selection rule due to exciton (elastic) scattering by impurities, interface, or alloy potential fluctuations.

In our analysis, we introduce the anisotropy of the exciton envelope function as an additional important parameter that affects the RRS profiles. This anisotropy defines the dimensionality of the exciton to be between two (for a strictly planar exciton) and three (for an exciton in a bulk crystal). By analyzing the RRS profiles we find that the BC $(e_B{:}\mathrm{hh}_B)1S$ and $(e_B{:}\mathrm{lh}_B)1S$ excitons are nearly two-dimensional (2D), as are the $(e_1{:}\mathrm{hh}_1)1S$ excitons of the SL sections forming the BCS. On the other hand, the excitons of a regular (nearly infinite) SL are nearly 3D, as are those of a bulk $\mathrm{Al}_{0.3}\mathrm{Ga}_{0.7}\mathrm{As}$ crystal. We also find that exciton scattering by potential fluctuations results in an increased intensity ratio between GaAs-like and AlAs-like LO-phonon Raman lines.

The paper is laid out as follows. Section II describes the quantum structures and the experimental results. Section III introduces the model and analysis of the RRS profiles and intensities. A short summary is given in Sec. IV.

II. EXPERIMENTAL PROCEDURE AND RESULTS

A. Structure

The BCS's, the SL, and the bulk crystal studied here were grown by molecular-beam epitaxy on (001)-oriented GaAs substrates. The two BCS's consist of finite $\mathrm{GaAs/Al}_{0.32}\mathrm{Ga}_{0.68}\mathrm{As}$ SL sections (five periods each) and wide $\mathrm{Al}_{0.32}\mathrm{Ga}_{0.68}\mathrm{As}$ spacer layers. The "unit cell" of these BCS's is shown in Fig. 1, and their parameters are summarized in Table I. The BCS unit cell is repeated 60 times. The SL was grown with the same parameters as the finite SL sections of the BCS, and its unit cell is repeated 300 times. The reference bulk crystal is a 5000-Å $\mathrm{Al}_{0.3}\mathrm{Ga}_{0.7}\mathrm{As}$ layer grown on a 5000-Å GaAs buffer layer. All samples are undoped and were grown without interruptions at the interfaces. The growth quality is essential for the phase coherence of the BC carriers, so that they fulfill the Bragg reflection condition at the interfaces between the SL sections and the $\mathrm{Al}_{0.32}\mathrm{Ga}_{0.68}\mathrm{As}$ spacers.[1]

A structural characterization of the BCS's and the SL samples was done by high-resolution x-ray diffraction. The diffractometer has a four-crystal monochromator, consisting of two U-shaped germanium crystals [(220) reflections], which yield a clean monochromatic ($\lambda=1.5406$ Å, $d\lambda/\lambda=10^{-4}$) symmetric beam profile, with a full width at half maximum of 12 arcsec.

The small lattice mismatch between $\mathrm{Al}_x\mathrm{Ga}_{1-x}\mathrm{As}$ and GaAs results in a very weak strain modulation throughout the samples. Therefore, in order to detect the BCS structural details, the (002) reflection was chosen due to the significant difference between the structure factors of GaAs and $\mathrm{Al}_x\mathrm{Ga}_{1-x}\mathrm{As}$ for this reflection. Figure 2 (curves *a*, *c*, and *e*) shows the measured (002) diffraction patterns of BCS A, BCS B, and the SL, respectively. Their corresponding optimally simulated patterns are shown in Fig. 2 (curves *b*, *d*, and *f*). They are calculated by using the dynamical diffraction theory, based on the solution of the Takagi-Taupin equations.[14,15] This is done in the following way: The x-ray diffraction of the SL and the BCS's shows clear satellite peaks, associated with the main (002) reflection of the bulk crystal. From the angular spacing between these peaks, the SL and the BCS periods are derived. The average lattice parameter is calculated from the angular separation of the zero-order SL (or BCS) peak and the substrate peak [unresolved in Fig. 2 (curves *a*, *c*, and *e*)]. The fine details of the structure were obtained by fitting the simulated diffraction patterns to the experimental ones. The period and average lattice parameter of each sample, deduced from the experimental data, are used as constraints on the input parameters of the simulation program. No apparent strain relaxation was observed within the measurement resolution, and the structures seem to be completely coherently strained.

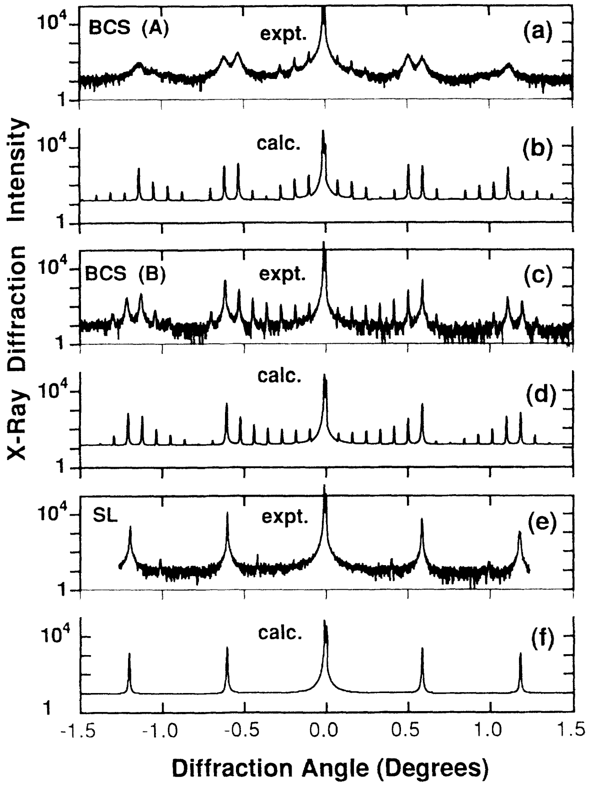

FIG. 2. A comparison between the observed and the calculated x-ray-diffraction patterns of the structures studied here. Curves (*a*), (*c*), and (*e*) show the measured diffraction patterns of BCS A, BCS B, and the SL, respectively. Curves (*b*), (*d*), and (*f*), present their corresponding calculated patterns. All intensities are given in a logarithmic scale.

An intrinsic property of any binary-ternary structure with a common group-V element is that a sharp transition from one material to the other cannot be defined. At least a one monolayer undefined transition layer exists at the heterointerface. Thus the values obtained here can be assumed to be exact within two monolayers. Another indication that the layer thickness fluctuates by no more

TABLE I. A comparison between the designed and measured parameters of the BCS's and SL under study. All layer width units are in Å.

Parameter		BCS A	BCS B	SL
d_w	designed	22.64	22.64	22.64
	measured	22(±3)	21(±3)	21(±3)
d_b	designed	62.26	62.26	62.26
	measured	60(±3)	58(±3)	57(±3)
d_s	designed	186.8	124.52	
	measured	180(±3)	121(±3)	
Λ	designed	84.9	84.9	84.9
	measured	82(±4)	79(±4)	78(±4)
Δ	designed	549.0	571.7	
	measured	530(±10)	537(±11)	
$x(\%)$	designed	32	32	32
	measured	32.5(±0.1)	32.3(±0.1)	32.3(±0.1)

than 1–2 monolayers is the small broadening of the higher-order satellites (less than 20 arcsec). In Table I we compare the layer widths of the designed BCS's and SL with those obtained by our fitting procedure.

B. Spectroscopy

For spectroscopic measurements, the samples were placed in an immersion-type dewar (at $T=2$ K) and excited by cw dye lasers pumped with an Ar^+ laser. The dye laser linewidth was 0.1 meV, and the intensity at the sample surface was varied in the range of 0.1–20 W/cm^2. A backscattering geometry was used, and the scattered radiation was dispersed by a double monochromator (resolution of 0.05 meV). Figure 3 shows the (incoming beam) LO-phonon RRS spectra of BCS A (curves *a* and *c*), BCS B (curves *b* and *d*), the SL (curve *e*) and the bulk $Al_{0.3}Ga_{0.7}As$ (curve *f*). Both the GaAs-like (at ~36 meV) and AlAs-like (at ~47 meV) LO-phonon branches are observed. Table II summarizes the LO-phonon Raman shifts for the different structures and for excitation at the exciton bands as shown in Figs. 3 (curves *a*–*f*). The differences between the LO-phonon spectral features and Raman shifts that are excited at different exciton bands of BCS A and BCS B clearly show that the LO phonons involved correspond to different spatial parts (either the $Al_{0.32}Ga_{0.68}As$ spacer layer or the SL sections) of the same BCS.[2]

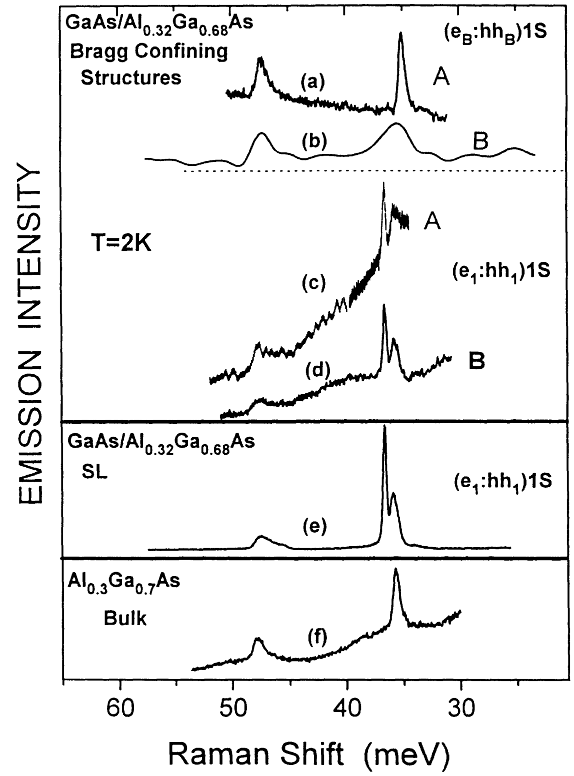

FIG. 3. A comparison between the incoming beam, LO-phonon Raman spectra of all the structures studied here at different exciton bands. Curves (*a*)–(*d*) correspond to BCS's A and B. Curve (*e*) corresponds to the SL, and (*f*) to the bulk $Al_{0.3}Ga_{0.7}As$. The incident laser energies are (a) 1.983 eV, (b) 1.995 eV, (c) 1.758 eV, (d) 1.761 eV, (e) 1.759 eV, and (f) 1.951 eV. The lines around $\hbar\omega_{LO}=35$ and 48 meV are the GaAs- and AlAs-like LO phonons, respectively.

The GaAs-like LO-phonon RRS profiles of the BCS's A and B, measured in the spectral range of the BC $(e_B\text{:hh}_B)1S$ and $(e_B\text{:lh}_B)1S$ excitons, are shown in Figs. 4(c) and 4(f), respectively. Also shown are the PL [Figs. 4(b) and 4(e)] and their PLE spectra [Figs. 4(a) and 4(d)], monitored at the $(e_B\text{:hh}_B)1S$ exciton bands.

TABLE II. A comparison between the measured LO-phonon Raman shifts, at different exciton bands, of the BCS's, the SL, and the bulk $Al_{0.3}Ga_{0.7}As$ under study.

Structure	Exciton band	E_{LO} (GaAs-like) (meV)	E_{LO} (AlAs-like) (meV)
BCS A	$(e_B\text{:hh}_B)1S$	35.1	47.4
	$(e_1\text{:hh}_1)1S$	36.6(1)/35.8(23)	47.7
BCS B	$(e_B\text{:lh}_B)1S$	35.4	47.3
	$(e_1\text{:hh}_1)1S$	36.6(1)/35.8(2)	47.6
SL	$(e_1\text{:hh}_1)1S$	36.6(1)/35.8(2)	47.5
Bulk $Al_{0.3}Ga_{0.7}As$	$(e\text{:hh})1S$	35.8	47.9

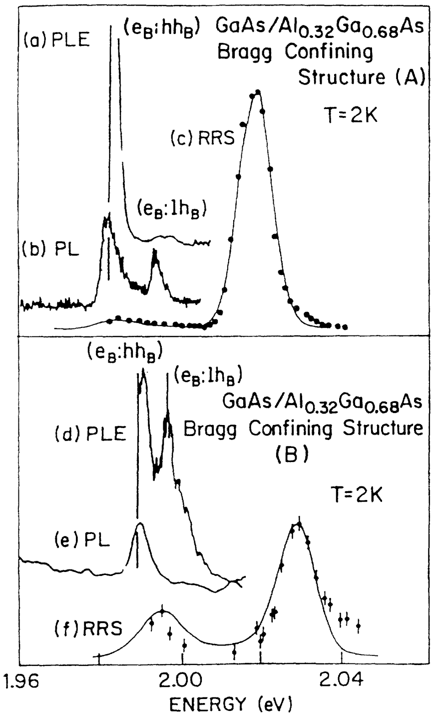

FIG. 4. (a) and (d) PLE spectra of BCS's A and B. The vertical bars denote the monitored emission energies. (b) and (e) PL spectra of BCS's A and B (excited at $E_l=2.075$ eV). (c) and (f) The GaAs-like LO-phonon RRS profiles of BCS's A and B, respectively. The solid lines in (c) and (f) are the model calculations (with the parameters given in Table IV).

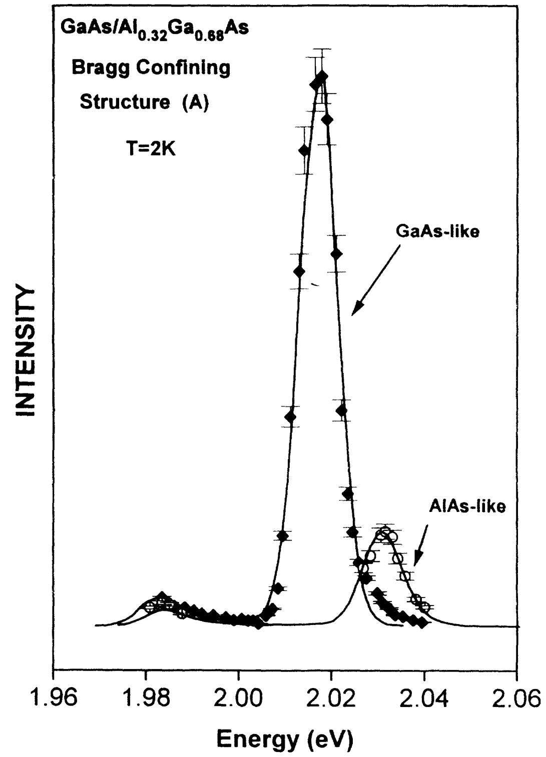

FIG. 6. A comparison between the RRS profiles of the GaAs- and AlAs-like LO phonons excited in the $(e_B\text{:hh}_B)1S$ and $(e_B\text{:lh}_B)1S$ exciton bands of BCS A. The experimental intensities are given by ♦ and ○ for the two types of LO phonons. The solid curves are the calculated RRS profiles.

For comparison purposes, we observed LO-phonon Raman scattering in the spectral range below the e_2 subband (corresponding to the range of the Bragg-confined exciton level in the BCS), in the SL. The scattering intensity is $\sim 10^{-5}$ and $\sim 10^{-3}$ weaker than that observed for BCS's A and B, respectively. Also, there is no resonant enhancement in this range. On the other hand, the PL and PLE spectra and the LO-phonon RRS profiles observed in the spectral range of the $(e_1\text{:hh}_1)1S$ exciton band are very similar in the BCS's and SL. (They were presented in Ref. 4).

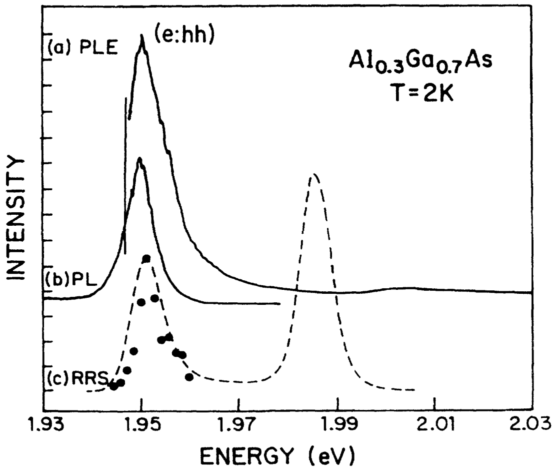

FIG. 5. The PL spectrum (b), its PLE spectrum (a), and the RRS profile (c) (full circles—observed, dashed line—calculated), of a bulk $Al_{0.3}Ga_{0.7}As$. (Only the calculated OB resonance is given. The intensity of the scattered light in this range is too weak to be resolved from the PL tail.)

Figure 5 shows the PL (curve a) and its PLE (curve b) spectra, in the spectral range of the lowest exciton band of the bulk $Al_{0.3}Ga_{0.7}$ As sample. The incoming beam (IB) LO-phonon RRS profile is shown in curve c. [The outgoing (OB) intensity is too weak to be resolved from the PL tail].

The difference between the OB and IB RRS intensities, excited in the $(e_B\text{:hh}_B)$ exciton spectral range, for BCS A, is demonstrated by the RRS profiles of the two types of LO phonons (Fig. 6). (Similar results are obtained for BCS B). It is noted that the ratio between the GaAs-like and the AlAs-like LO-phonon RRS intensities is much greater in the OB channel than in the IB channel.

III. MODEL AND ANALYSIS

Our aim is to analyze the RRS profiles observed in the spectral ranges of the $(e_1\text{:hh}_1)1S$, $(e_B\text{:hh}_B)1S$, and $(e_B\text{:lh}_B)1S$ exciton bands. In particular we will analyze the spectral shape of the RRS profile and the OB/IB intensity ratio. The model is based on excitons being the intermediate states in the light-scattering process. However, we do not have the exact form of the exciton wave functions. Therefore, we will use a trial function that separates the internal degrees of freedom from the translational ones. In this way we will show that the anisotropy of the exciton 1*S* wave function (i.e., the relative *e-h* motion) strongly affects the exciton–LO-phonon interaction. The translational part will depend on the detailed structure (SL or BCS). For these we will adapt the *e* and *h* wave functions that are obtained by effective-mass-approximation (EMA) calculations.[1,4] Figure 7 presents the BC probability densities, calculated for the e_B, hh_B, and lh_B envelope functions $|\chi(z)|^2$ for BCS A. Using these functions, the degree of Bragg confinement is calculated as

$$\Upsilon_B \equiv \frac{\int_{-d_s/2}^{d_s/2} |\chi(z)|^2 dz}{\int_{-\Delta/2}^{\Delta/2} |\chi(z)|^2 dz} , \tag{1}$$

and the overlap integral between the *e* and *h* envelope functions is calculated as

$$O \equiv \int_{-\Delta/2}^{\Delta/2} \chi_e^*(z)\chi_h(z) dz . \tag{2}$$

(*h* represents either hh or lh). The values of Υ and $|O|^2$ for the e_B, hh_B, and lh_B in BCS's A and B are given in Table III. It is clearly seen that the e_B, lh_B, and especially hh_B are less confined in BCS B than in BCS A. High values of Υ and $|O|^2$ mean that there is a small transfer rate from a BC state to a SL section confined state. This will be shown to have a significant effect on the RRS profile and on its intensity. Since we will calculate the RRS profiles for excitation in the (e_1:hh_1) spectral range, we show the calculated $|\chi(z)|^2$ for the $e_1(1)-e_1(5)$ states for BCS A (Fig. 8). Similar distributions are calculated for BCS B. For both BCS's, $|\chi(z)|^2$ of the hh_1 and lh_1 states are quite similar to the e_1 states.

TABLE III. Calculated degrees of confinement Υ and square overlap integrals $|O|^2$ of BC *e* and *h* states at BCS's A and B.

Structure	$\Upsilon(e_B)$	$\Upsilon(\mathrm{hh}_B)$	$\Upsilon(\mathrm{lh}_B)$	$\lvert O\rvert^2(e_B{:}\mathrm{hh}_B)$	$\lvert O\rvert^2(e_B{:}\mathrm{lh}_B)$
BCS A	0.97	0.91	0.95	0.932	0.998
BCS B	0.92	0.69	0.89	0.802	0.997

The LO-phonon RRS amplitude is generally given by[16]

$$A_{fi} = \sum_{j,m} \frac{(H_{\mathrm{ER}})_{fj}(H_{\mathrm{EL}})_{jm}(H_{\mathrm{ER}})_{mi}}{(E_l - E_m + i\Gamma_m)(E_s - E_j + i\Gamma_j)} \times \delta[E_l(\mathbf{k}_l) - E_s(\mathbf{k}_2) - \hbar\omega_{\mathrm{LO}}(\mathbf{Q})] . \tag{3}$$

E_j and E_m are the energies of the intermediate exciton states that have Γ_j and Γ_m as phenomenological damping coefficients. H_{ER} and H_{EL} are the exciton-radiation and the exciton–LO-phonon (Fröhlich) interactions, respectively. E_l, E_s, and $\hbar\omega_{\mathrm{LO}}$ are the energies of the incident photon, scattered photon, and LO phonon, respectively. $\mathbf{k}_l$, $\mathbf{k}_s$, and $\mathbf{Q}$ are the corresponding wave vectors.

Only 1*S* exciton states are considered since they have a much stronger coupling to the photons than higher *nS* states. (The excitonic oscillator strength falls as $\sim 1/n^3$.) In addition, we neglect the LO-phonon dispersion [i.e., $\hbar\omega_{\mathrm{LO}}(\mathbf{Q}) \approx \hbar\omega_{\mathrm{LO}}(0)$] and the folded branch structure.

For the unperturbed 1*S* excitons, in all the cases studied here, we use

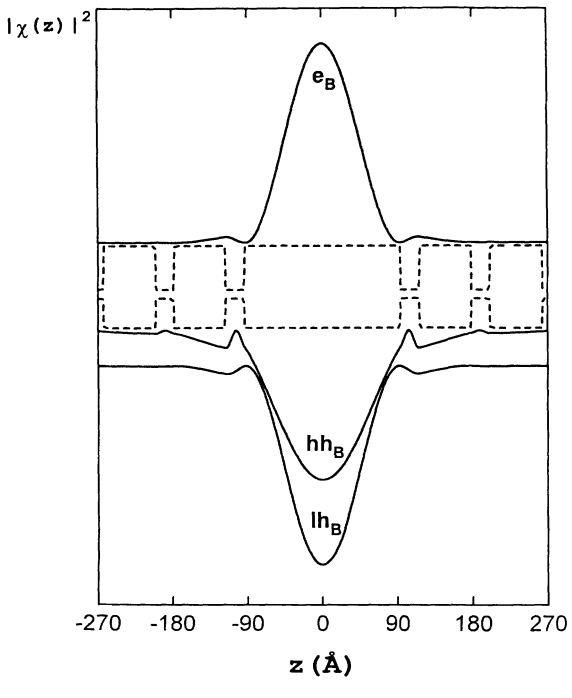

FIG. 7. Calculated probability densities $|\chi(z)|^2$ of e_B, hh_B, and lh_B, for BCS A.

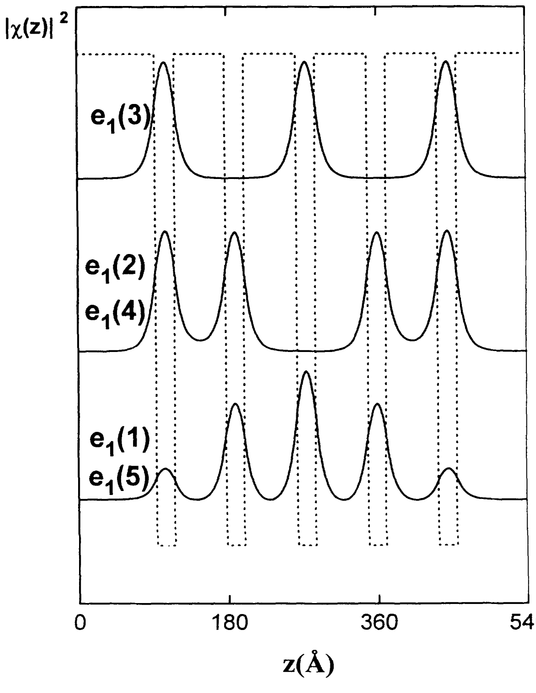

FIG. 8. Calculated probability densities $|\chi(Z)|^2$ of $e_1(1)-e_1(5)$ subbands of the superlattice sections of BCS A.

$$\Psi^{(0)}_{\mathbf{K}_\parallel,K_z}(r_\parallel,\mathbf{R}_\parallel,z,Z) = \frac{1}{\sqrt{\pi a_\parallel^2 a_z S}} \exp\left\{-\left[\left[\frac{r_\parallel}{a_\parallel}\right]^2+\left[\frac{z}{a_z}\right]^2\right]^{1/2}\right\} \times e^{i\mathbf{K}_\parallel\cdot\mathbf{R}_\parallel} f_{K_z}(Z)\,. \tag{4}$$

The part that depends on the relative *e-h* coordinates $(\mathbf{r}_\parallel, z)$ is the commonly used anisotropic 1*S* trial function.[17,18] The ratio between the in-plane Bohr radius $(a_\parallel)$ and that along the growth direction (a_z) defines the exciton dimensionality. $a_\parallel$ and a_z are the parameters that will be obtained by fitting the model calculated to the observed RRS profiles. *S* is the quantization area. The part that describes the exciton center of mass (c.m.) motion $(R_\parallel, Z)$ is factored out as a plane wave, with an in-plane wave vector $\mathbf{K}_\parallel$, and an envelope wave function $f_{K_z}(Z)$ that depends on the c.m. coordinate and wave vector along the confinement direction. For the $(e_B\text{:hh}_B)1S$ case, $f_{K_z}(Z)$ describes an exciton that is tightly confined in the spacer layer of the BCS. We use the e_B envelope functions shown in Fig. 7 as an approximated exciton wave function $f_{K_z}(Z)$. For the finite SL sections of the BCS, the five $f_{K_z}(Z)$ functions that describe the $[e_1(1-5)\text{:hh}_1]1S$ exciton c.m. motion along the confinement direction are approximately taken as the $e_1(1-5)$ envelope functions (Fig. 8). The splitting of these five states is resolved in the RRS profile.[4] For the fully periodic SL, there is a quasicontinuous dispersion of the $(e_1\text{:hh}_1)1S$ exciton miniband along K_Z, thus f_{K_z} is approximated as an extended wave, $f_{K_z}(Z) \sim e^{iK_z Z}$.

In the parabolic band approximation, the $(e_1\text{:hh}_1)1S$, $(e_B\text{:hh}_B)1S$, or $(e_B\text{:lh}_B)1S$ exciton energy dispersion is given by

$$E_{1S}(K_\parallel,K_Z) \approx E^0_{1S} + \frac{\hbar^2 K_\parallel^2}{2M_\parallel} + \frac{\hbar^2 K_Z^2}{2M_Z}\,, \tag{5}$$

where

$$M_\parallel = m_{e\parallel} + m_{\text{hh}\parallel}\,, \tag{6}$$

$$M_Z = m_{ez} + m_{\text{hh}z}\,,$$

$$E^0_{1S} = E_e + E_{\text{hh}} - E_b\,. \tag{7}$$

E_b is the exciton binding energy. It is assumed that, in general, the exciton has an anisotropic mass and in the limit of a fully confined state $M_Z \to \infty$.

As Eq. (3) shows, the resonant poles of the RRS amplitude are at $E_l = E_m$ (IB) and $E_s = E_j$ (OB), with E_m and E_j given by the appropriate values of Eq. (5). Energy conservation requires that $E_s = E_l - \hbar\omega_{\text{LO}}$.

In an ideal semiconductor, the exciton c.m. wave vector $\mathbf{K}$ is a good quantum number. Since the exciton is excited by an optical photon, $\mathbf{K} \sim \mathbf{0}$. Therefore, the strength of the IB resonance, in which $E_l = E^0_{1S}$, is expected to be equal to that of the OB resonance $(E_s = E^0_{1S})$. However, since most of the RRS experiments in semiconductor QW's and alloys show that the OB is stronger than the IB, various mechanisms of $\mathbf{K}$ nonconservation were suggested.[8-13] Random scattering of the excitons from potential fluctuations induced by alloy disorder and interface roughness have been proposed as the main physical mechanisms.

For the scattering potential we assume randomly distributed, uncharged point centers that represent both alloy and interface fluctuations. Each center gives rise to the following perturbation Hamiltonian, operating only on the c.m. part of the exciton wave function:

$$H_s(\mathbf{R}_\parallel, Z) = V_0 \delta(\mathbf{R}_\parallel - \mathbf{R}^0_\parallel)\delta(Z - Z^0)\,. \tag{8}$$

$(\mathbf{R}^0_\parallel, Z^0)$ are the position coordinates of the center. A single scattering event per exciton is considered. The intrinsic exciton degrees of freedom are assumed to be unperturbed, and since the scattering center is very heavy, the small shift of the exciton c.m. energy is neglected.

Without a loss of generality, we can shift the exciton c.m. coordinates to $(\mathbf{R}^0_\parallel, Z^0)$, and by assuming the Born approximation the perturbed exciton wave function which consists of a wave packet centered at $(\mathbf{K}_\parallel, k_Z)$ can formally be written in terms of the unperturbed wave functions:

$$\Psi_{\mathbf{K}_\parallel,K_Z} = \int_{BZ_\parallel} \frac{d^2K'_\parallel}{(2\pi)^2} \int_{BZ_Z} \frac{dK'_Z}{2\pi} \Psi^{(0)}_{\mathbf{K}'_\parallel,K'_Z}[\delta(\mathbf{K}'_\parallel - \mathbf{K}_\parallel)\delta(K'_Z - K_Z) + g(K_\parallel, K'_\parallel, K_Z, K'_Z)]\,. \tag{9}$$

$g(K_\parallel, K'_\parallel, K_Z, K'_Z)$ is the Born propagator. Since the exciton in-plane translational mass $(M_\parallel)$ is much smaller than that along the confinement direction (M_Z), the propagator corresponding to H_s of Eq. (8) can be approximated by

$$g(K_\parallel, K'_\parallel, K_Z, K'_Z) \approx \frac{2M_\parallel V_0}{\hbar^2} \frac{f_{K_Z}(0) f^*_{K'_Z}(0)}{K_\parallel^2 - K'^2_\parallel}\,. \tag{10}$$

Then, the integral in Eq. (9) yields

$$\Psi_{\mathbf{K}_\parallel,K_Z} = \frac{1}{\sqrt{\pi a_\parallel^2 a_z S}} \exp\left\{-\left[\left[\frac{r_\parallel}{a_\parallel}\right]^2+\left[\frac{z}{a_z}\right]^2\right]^{1/2}\right\} \times \left[e^{i\mathbf{K}_\parallel\cdot\mathbf{R}_\parallel} f_{K_Z}(Z) - \frac{i}{4}\frac{2M_\parallel V_0 B(Z)}{\hbar^2} f_{K_Z}(0) H_0^{(1)}(K_\parallel R_\parallel) \right]\,, \tag{11}$$

where

$$B(Z)=\int_{BZ_Z}\frac{dK_Z}{2\pi}f^*_{K_Z}(0)f_{K_z}(Z)\ , \tag{12}$$

and $H_0^{(1)}(K_\parallel R_\parallel)$ is the zeroth-order Hankel function of the first degree.

For a confined exciton, the dispersion along K_Z is negligible and therefore $B(Z)\approx f_{K_Z}(Z)e^{-iK_ZZ}\mathrm{sinc}[(\pi/\Delta)Z]$. However, since $\mathrm{sinc}[(\pi/\Delta)Z]$ varies much more slowly relative to $f_{K_Z}(Z)$, in the confinement interval $B(Z)\sim f_{K_Z}(Z)e^{-iK_ZZ}=U_{K_Z}(Z)$, where $U_{K_Z}(Z)$ is the Bloch amplitude of $f_{K_Z}(Z)$. Moreover, for a tightly confined exciton $U_{K_Z}(Z)\sim\delta(Z)$. Thus the scattering amplitude [which is the second term of Eq. (11)] describes a purely in-plane evanescent wave. On the other hand, for an extended exciton (as in a bulk material or in a SL) $f_{K_Z}(Z)\approx e^{iK_ZZ}$ and $B(Z)\propto\mathrm{sinc}[(\pi/\Lambda)Z]$, where Λ is the SL period or the bulk lattice constant. In this case, the scattering amplitude describes a three-dimensional evanescent wave.

Now we turn to calculate the matrix elements appearing in Eq. (3). The initial and final excitonic states are the crystal ground state, $|g\rangle$, and the intermediate states are the perturbed exciton wave packets [Eq. (11)] with $|m\rangle\equiv|\mathbf{K}_\parallel^{(m)},K_Z^{(m)}\rangle$, and similarly for $|j\rangle$. Then,

$$A(E_l,E_s,\mathbf{Q})=\sum_{j,m}\frac{(H_{\mathrm{ER}})_{gj}(H_{\mathrm{EL}}(\mathbf{Q}))_{jm}(H_{\mathrm{ER}})_{mg}\delta(E_l-E_s-\hbar\omega_{\mathrm{LO}})}{[E_l-E_{1S}(m)+i\Gamma_{1S}(m)][E_s-E_{1S}(j)+i\Gamma_{1S}(j)]}\ . \tag{13}$$

In the electric dipole approximation, the exciton-photon matrix element is[19]

$$(H_{\mathrm{ER}})_{mg}\approx\frac{ieF\hbar}{2m_0E_l}\langle m|\boldsymbol{\epsilon}_l\cdot\mathbf{p}|g\rangle \tag{14}$$

$$=\frac{ieF\hbar P_{vc}}{2\sqrt{2m_0E_l}}\frac{1}{\sqrt{\pi a_\parallel^2a_z}}\left[\delta(\mathbf{K}_\parallel^{(m)})\phi(K_Z^{(m)})+\frac{2M_\parallel V_0\Xi}{\hbar^2}\frac{1}{(K_\parallel^{(m)})^2}f_{K_Z^{(m)}}(0)\right]\ . \tag{15}$$

F is the photon electric-field amplitude, and $\boldsymbol{\epsilon}_l$ is its polarization vector, m_0 and e are the free-electron mass and charge. P_{vc} is the interband dipole matrix element.

The function $\phi(K_Z^{(m)})$ is given by

$$\phi(K_Z^{(m)})=\int_{\text{unit cell}}dZ\,f_{K_Z^{(m)}}(Z)\ , \tag{16}$$

where the integration is over a unit cell along the growth direction (namely for a BCS it is the period Δ, and for a SL a period Λ, cf. Fig. 1). $\phi(K_Z^{(m)})\sim1$ for a tightly localized exciton state, while for an extended exciton $\phi(K_Z^{(m)})\sim\delta(K_Z^{(m)})$. Ξ is a constant, given by

$$\Xi=\int_{BZ_Z}\frac{dK_Z}{2\pi}\phi(K_Z)f^*_{K_Z}(0)\ . \tag{17}$$

A similar expression is written for $(H_{\mathrm{ER}})_{gj}$, with $(m)\to(j)$ and $E_l\to E_s$.

The separation between the internal and c.m. excitonic motion simplifies the calculation of the RRS amplitude, since the Fröhlich interaction acts only on the internal coordinates, while the potential fluctuations act only on the c.m. coordinates. For the calculation of the Fröhlich interaction matrix element we then use a quasi-three-dimensional Hamiltonian[20]

$$H_{\mathrm{EL}}(\mathbf{Q})=\frac{C_F}{|\mathbf{Q}|}(e^{i\mathbf{Q}\cdot\mathbf{r}_{\mathrm{e}}}-e^{i\mathbf{Q}\cdot\mathbf{r}_{\mathrm{h}}})\ . \tag{18}$$

C_F is the Fröhlich interaction coupling constant. The anisotropy is entered via the c.m. transformation of $\mathbf{r}_{\mathrm{e}}$ and $\mathbf{r}_{\mathrm{h}}$:

$$\mathbf{r}_{\mathrm{e}}=\left[\mathbf{R}_\parallel+\frac{m_{h\parallel}}{M_\parallel}\mathbf{r}_\parallel,Z+\frac{m_{hz}}{M_Z}z\right]\ ,$$
$$\mathbf{r}_{\mathrm{h}}=\left[\mathbf{R}_\parallel-\frac{m_{e\parallel}}{M_\parallel}\mathbf{r}_\parallel,Z-\frac{m_{ez}}{M_Z}z\right]\ . \tag{19}$$

After some algebra, we obtain

$$\begin{aligned}(H_{\mathrm{EL}}(\mathbf{Q}))_{jm}&=\langle 1S(\mathbf{K}_\parallel^{(j)},K_Z^{(j)}),1_{\mathrm{LO}}|H_{\mathrm{EL}}|1S(\mathbf{K}_\parallel^{(m)},K_Z^{(m)}),0_{\mathrm{LO}}\rangle\\&\approx\frac{C_F}{Q}[\alpha(\xi_{\mathrm{e}})-\alpha(\xi_{\mathrm{h}})][\delta(\mathbf{K}_\parallel^{(j)}-\mathbf{K}_\parallel^{(m)}-\mathbf{Q}_\parallel)\Theta(K_Z^{(m)},K_Z^{(j)},Q_Z)\ .\\&\quad+\frac{2M_\parallel V_0}{\hbar^2}\left[\frac{1}{(K_\parallel^{(m)})^2-|\mathbf{K}_\parallel^{(j)}+\mathbf{Q}_\parallel|^2}+\frac{1}{(K_\parallel^{(j)})^2-|\mathbf{K}_\parallel^{(m)}-\mathbf{Q}_\parallel|^2}\right]\ ,\end{aligned} \tag{20}$$

where we neglected the higher-order terms in V_0 (in order to be consistent with the Born approximation).

$$\xi_{\parallel}^{i}=\frac{m_{\parallel}^{i}a_{\parallel}Q_{\parallel}}{2M_{\parallel}}\ ,\qquad \xi_{z}^{i}=\frac{m_{z}^{i}a_{z}Q_{Z}}{2M_{Z}}\ . \tag{21}$$

(The index i refers to e, hh, or lh).

The function $\alpha(\xi)$ depends on the exciton dimensionality[17]

$$\alpha(\xi)\propto(1+|\xi|^{2})^{-p}\ , \tag{22}$$

where $p=\frac{3}{2}$ for the purely two-dimensional case, and $p=2$ for the purely three-dimensional case or for a small exciton anisotropy (as for a 1S exciton in a SL). The Fröhlich interaction form factor is given by

$$F(\mathbf{Q})=\frac{C_F}{|\mathbf{Q}|}[\alpha(\xi_e)-\alpha(\xi_{\rm hh})]\ , \tag{23}$$

and similarly for lh.

The function $\Theta(K_Z^{(m)},K_Z^{(j)},Q_Z)$ is given by

$$\begin{aligned}\Theta(K_Z^{(m)},K_Z^{(j)},Q_Z)&=\int_{\text{unit cell}}f^{*}_{K_Z^{(m)}}(Z)f_{K_Z^{(j)}}(Z)e^{iQ_ZZ}dZ\\&=\int_{\text{unit cell}}U^{*}_{K_Z^{(m)}}(Z)U_{K_Z^{(j)}}(Z)e^{i(Q_Z+K_Z^{(j)}-K_Z^{(m)})Z}dZ\ .\end{aligned} \tag{24}$$

Again, the unit cell length is Δ or Λ for the BCS or SL, respectively. $\Theta(K_Z^{(m)},K_Z^{(j)},Q_Z)\rightarrow 1$ for a 2D exciton, while for a 3D exciton $\Theta(K_Z^{(m)},K_Z^{(j)},Q_Z)\rightarrow\delta(K_Z^{(m)}-K_Z^{(j)}-Q_Z)$.

The contribution of the two exciton states with energies of $E_{1S}(\mathbf{K}_{\parallel}=0)$ and $E_{1S}(\mathbf{K}_{\parallel})=E_{1S}(\mathbf{K}_{\parallel}=0)+(\hbar^2K_{\parallel}^2/2M_{\parallel})$ to the scattering amplitude is then given by

$$\begin{aligned}A(E_l,E_s,\mathbf{Q})=&-\frac{e^2\hbar^2F^2}{8m_0^2}\frac{|P_{vc}|^2}{(\pi a_{\parallel}^2a_{\perp})}\frac{1}{E_lE_s}F(\mathbf{Q})\delta(E_l-E_s-\hbar\omega_{\rm LO})\\&\times\Bigg\{\frac{\delta(\mathbf{Q}_{\parallel})\eta(Q_Z)}{[E_l-E_{1S}(0)+i\Gamma_{1S}(0)][E_s-E_{1S}(0)+i\Gamma_{1S}(0)]}\\&+\frac{2M_{\parallel}V_0}{\hbar^2Q_{\parallel}^2}\Bigg[\Xi X(Q_Z)\Bigg\{\frac{1}{[E_l-E_{1S}(Q_{\parallel})+i\Gamma_{1S}(Q_{\parallel})][E_s-E_{1S}(0)+i\Gamma_{1S}(0)]}\\&\qquad+\frac{1}{[E_l-E_{1S}(0)+i\Gamma_{1S}(0)][E_s-E_{1S}(Q_{\parallel})+i\Gamma_{1S}(Q_{\parallel})]}\Bigg\}\\&-\frac{2Y(Q_Z)}{[E_l-E_{1S}(0)+i\Gamma_{1S}(0)][E_s-E_{1S}(0)+i\Gamma_{1S}(0)]}\Bigg]\Bigg\}\ .\end{aligned} \tag{25}$$

The functions $\eta(Q_Z)$, $X(Q_Z)$, and $Y(Q_Z)$ are given by

$$\begin{aligned}\eta(Q_Z)&=\int_{BZ_Z}\frac{dK_Z^{(m)}}{2\pi}\int_{BZ_Z}\frac{dK_Z^{(j)}}{2\pi}\phi(K_Z^{(m)})\phi(K_Z^{(j)})\Theta(K_Z^{(m)},K_Z^{(j)},Q_Z)\ ,\\X(Q_Z)&=\int_{BZ_Z}\frac{dK_Z^{(m)}}{2\pi}\int_{BZ_Z}\frac{dK_Z^{(j)}}{2\pi}\phi(K_Z^{(m)})f_{K_Z^{(j)}}(0)\Theta(K_Z^{(m)},K_Z^{(j)},Q_Z)\ ,\\Y(Q_Z)&=\int_{BZ_Z}\frac{dK_Z^{(m)}}{2\pi}\int_{BZ_Z}\frac{dK_Z^{(j)}}{2\pi}\phi(K_Z^{(m)})\phi(K_Z^{(j)})\ .\end{aligned} \tag{26}$$

$\eta(Qz)\rightarrow 1$, for a 2D exciton limit, while in the 3D limit $\eta(Q_Z)\rightarrow\delta(Q_Z)$. In both 2D and 3D limits $X(Q_Z),Y(Q_Z)\rightarrow 1$.

The exciton bands are inhomogeneously broadened: we take a Gaussian distribution $\rho(E_{1S}(0))$ (with a width $2\sqrt{\ln 2}\Delta$) for the spectral distribution of E_{1S}. The RRS profile is then given by[2]

$$\sigma(E_l)=\sigma_0\int_{BZ_{\parallel}}\frac{d^2Q_{\parallel}}{(2\pi)^2}\int_{BZ_Z}\frac{dQ_Z}{(2\pi)}\int dE_{1S}(0)\rho(E_{1S}(0))|A(E_l,E_s,\mathbf{Q})|^2\ . \tag{27}$$

The exciton damping factors Γ_{1S} have a spectral distribution over the exciton band.[13] However, the calculated RRS profiles can be well fitted to the experimental ones assuming a single Γ_{1S} for each of the excitonic bands studied here. The fitting parameters used for calculating the RRS profiles are summarized in Table III. The sensitivity of the parameters to the best fit is ±5%. The calculated $\sigma(E_l)$ are shown by the solid lines and are compared to the observed RRS profiles (Figs. 4 and 5 and Ref. [4]).

A double resonance is obtained when the denominator in the second term of Eq. (25) satisfies

$$\begin{gathered} E_l = E_{1S}(\mathbf{Q}_\|) = E_{1S}(0) + \hbar\omega_{\mathrm{LO}}(\mathbf{Q}_\|) \\ \text{and} \\ E_s = E_{1S}(0)\ . \end{gathered} \tag{28}$$

That is schematically shown in Fig. 9. Denoting by $\mathbf{K}_{\|\mathrm{res}}$ and $\mathbf{Q}_{\mathrm{res}}$ the exciton and LO-phonon wave vectors that satisfy the resonance conditions, we have

$$\begin{gathered} \frac{\hbar^2 K_{\|\mathrm{res}}^2}{2M_\|} = \hbar\omega_{\mathrm{LO}}(Q_{\mathrm{res}})\ , \\ \mathbf{K}_{\|\mathrm{res}} - \mathbf{Q}_{\mathrm{res}} \approx 0\ . \end{gathered} \tag{29}$$

A *key point* of our model is the connection between the degree of *asymmetry* between the IB and OB resonances and the 1*S exciton dimensionality* ($a_\|/a_z$). As is shown in Fig. 9, the enhancement of the OB intensity, relative to that of the IB, is dependent on the probability for an exciton c.m. momentum transfer into values around $\hbar\mathbf{K}_{\|\mathrm{res}}$. This probability decreases sharply with an increased $K_{\|\mathrm{res}}$ [cf. Eq. (10)]. Thus, since $K_{\|\mathrm{res}} \propto \sqrt{M_\|}$ [Eq. (29)], the probability is inversely proportional to $M_\|$. In GaAs/Al$_x$Ga$_{1-x}$As QW's, the 2D "heavy hole" becomes lighter than the 3D heavy hole, and even lighter than the 2D "light hole." Near $\mathbf{K}_\| \sim 0$, we have[21,22] $M_\|(2\mathrm{D}) \approx \frac{1}{2} M_\|(3D)$. Therefore, the conditions for a double resonance are more favorable for a nearly 2D (e:hh)1S exciton.

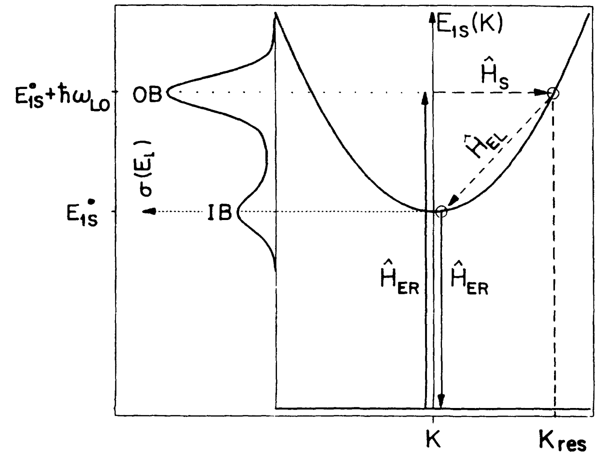

FIG. 9. A schematic description of the effect that an exciton momentum transfer by the random fluctuations potential $\hat{H}_S$ has on the RRS profile shape. The double resonance causes an asymmetric RRS profile (enhancement of the OB intensity relative to the IB intensity).

The (e_B:hh$_B$)1S exciton is much more confined in BCS A than in BCS B. The (e_B:lh$_B$)1S confinement is high for both BCS's. Therefore, we expect the RRS profile peaks (both OB and IB) to appear at the (e_B:hh$_B$)1S exciton band in BCS A and at the (e_B:lh$_B$)1S exciton band in BCS B. This is confirmed by comparing the observed PLE spectra with the RRS profiles as Figs. 4(b) and 4(c) and 4(e) and 4(f) show for BCS A and BCS B, respectively. In addition, the RRS intensity, in the spectral range of the BC excitons, is two orders of magnitude lower in BCS B than in BCS A. This is due to two factors: (a) a much more effective depopulation, (e_B:hh$_B$)1S $\rightarrow$(e_1:hh$_1$)1S, in BCS B, resulting from the low confinement of the (e_B:hh$_B$)1S exciton; (b) the (e_B:lh$_B$)1S exciton dephasing involves both (e_B:lh$_B$)1$S$$\rightarrow$($e_B$:hh$_B$)1$S$ and (e_B:lh$_B$)1$S$$\rightarrow$($e_1$:hh$_1$)1$S$ scattering channels.

A clear evidence of the influence of the scattering potential H_s on the RRS process is shown in Fig. 6. The intensity ratio between the Raman-scattering bands involving GaAs- and AlAs-like LO phonons, I_G/I_A, is much larger in the OB than in the IB, in both BCS's A and B. The measured ratio at the peaks of the RRS profiles is $(I_G/I_A)_{\mathrm{OB}}/(I_G/I_A)_{\mathrm{IB}} = 3.0 \pm 0.1$. This can be roughly explained by reexamining the OB resonance condition: $Q_{\mathrm{res}}^2 \propto \omega_{\mathrm{LO}}$ [Eq. (29)], and the resulting Fröhlich interaction form factor and RRS cross section [Eqs. (23), (25), and (27)]:

$$\sigma[E_l = E_{1S}(0) + \hbar\omega_{\mathrm{LO}}] \propto \left[\frac{F(\mathbf{Q}_{\mathrm{res}})}{Q_{\mathrm{res}}} \right]^2 \propto \left[\frac{F(\mathbf{Q}_{\mathrm{res}})}{\omega_{\mathrm{LO}}} \right]^2 . \tag{30}$$

Here we neglect the contribution of the off-resonant Q's. Then:

$$(I_G/I_A)_{\mathrm{OB}} \sim (I_G/I_A)_{\mathrm{IB}} \left[\frac{F(\mathbf{Q}_{\mathrm{res}}(\mathrm{GaAs}))}{F(\mathbf{Q}_{\mathrm{res}}(\mathrm{AlAs}))} \right]^2 \times \left[\frac{\omega_{\mathrm{LO}}(\mathrm{AlAs})}{\omega_{\mathrm{LO}}(\mathrm{GaAs})} \right]^2 . \tag{31}$$

Using the measured values of $\hbar\omega_{\mathrm{LO}}$(AlAs) and $\hbar\omega_{\mathrm{LO}}$(GaAs) (Table II) and their corresponding Q_{res}'s we obtain $(I_G/I_A)_{\mathrm{OB}} \sim 2.4$. A detailed calculation of the RRS profiles of the GaAs- and AlAs-like LO phonons (with the parameters given in Table IV) yields good agreement with experimental ones, as is demonstrated in Fig. 6.

Finally we note that OB resonance cannot be observed in the PL spectral range of the bulk Al$_{0.3}$Ga$_{0.7}$As crystal. This means that the OB/IB intensity ratio is much smaller than in all the BCS and SL excitons. From this we conclude that the confinement and large anisotropy of the latter structures are the main physical factors that differentiate between them and the bulk alloy.

Several conclusions can be drawn from the good fit to

TABLE IV. The parameters used in fitting the RRS profiles.

Structure	Exciton type	Γ_{1s} (meV)	$(\sqrt{\ln 2})\Delta$ (meV)	$a_\parallel$ (Å)	a_z (Å)	$\frac{M_\parallel}{m_0}$
BCS A	$[e_B{:}\mathrm{hh}_B]1S$	0.2	4.5	50	6	0.22
	$[e_B{:}\mathrm{lh}_B]1S$	0.5	4.5	60	15	0.30
	$[e_1(1){:}\mathrm{hh}_1]1S$	0.20	2.0	60	10	0.22
	$[e_1(2){:}\mathrm{hh}_1]1S$	0.20	2.0	60	10	0.22
	$[e_1(3){:}\mathrm{hh}_1]1S$	0.21	2.0	60	10	0.22
	$[e_1(4){:}\mathrm{hh}_1]1S$	0.25	2.0	60	10	0.22
	$[e_1(5){:}\mathrm{hh}_1]1S$	0.40	2.0	60	10	0.22
BCS B	$[e_B{:}\mathrm{hh}_B]1S$	1.5	4.5	70	30	0.35
	$[e_B{:}\mathrm{lh}_B]1S$	0.8	4.5	60	15	0.25
SL	$[e_1{:}\mathrm{hh}_1]1S$	0.20	3.5	60	20	0.35
$Al_{0.3}Ga_{0.7}As$ (Bulk)	$[e{:}\mathrm{hh}]1S$	0.30	3.7	95[a]		0.47[a]

[a] These are three-dimensional (isotropic) parameters.

the experimental RRS profiles.

(a) The large anisotropy in the $(e_B{:}\mathrm{hh}_B)1S$ exciton wave function of BCS A ($a_\parallel/a_z \sim 8$) indicates that this exciton is virtually two dimensional. The other BC excitons have smaller anisotropies (cf. Table. IV).

The confinement factors of the BC excitons are similar to those calculated[18] for $(e_1{:}\mathrm{hh}_1)1S$ excitons in conventional $GaAs/Al_xGa_{1-x}As$ QW's. In the latter case, the calculated $a_\parallel/a_z \sim 4.5$, for a well width similar to the Bragg confining spacer layers of BCS A. From this we conclude that the exciton dimensionality is largely determined by the degree of confinement. As the degree of confinement decreases, and the exciton wave function spreads over large distances, its dimensionality approaches 3: In the finite SL sections $a_\parallel/a_z \sim 6$, while in the fully periodic SL $a_\parallel/a_z \sim 3$ (cf. Table IV).

(b) In BCS B the heavy hole is not Bragg confined (the calculated confinement probability is $\sim 70\%$). Therefore, as is shown in Fig. 4(f), both the IB and OB most intense peaks are at the $(e_B{:}\mathrm{lh}_B)1S$ exciton band. The low RRS intensities indicate that there is a fast relaxation, mainly to the extended $(e_B{:}\mathrm{hh}_B)1S$ exciton states.

(c) The exciton damping factors obtained in fitting all the RRS profiles are small. For the five $[e_1(1-5){:}\mathrm{hh}_1]1S$ exciton bands of the SL sections, Γ_{1S} gradually increases with increasing energy. This means that the damping processes are the exciton relaxation between the five bands, most probably by acoustic-phonon scattering.[12] The $(e_B{:}\mathrm{hh}_B)$ exciton, of BCS A, has the same Γ_{1S} as the lowest exciton of the SL section, indicating that any additional damping mechanisms (due to its high energy) are slow relative to the acoustic-phonon scattering.

IV. SUMMARY

We compared the LO-phonon resonant Raman-scattering profiles, excited in the various exciton spectral ranges of three types of semiconductors structures: Two $GaAs/Al_{0.32}Ga_{0.68}As$ Bragg-confining structures, a superlattice, and a bulk $Al_{0.3}Ga_{0.7}As$ crystal. All the quantum structures have the same SL dimensions. The RRS profiles are examined with regard to the outgoing-beam to incoming-beam intensity ratio, their spectral positions compared to the PL and PLE bands, and their bandwidth. The analysis is done by using a model based on the following assumptions: (a) The exciton translational motion is described by a wave packet resulting from the exciton scattering by interface roughness or alloy fluctuations. The scattering centers are assumed to be neutral point centers that affect only the translational exciton motion. (b) The exciton–LO-phonon (Fröhlich) interaction depends on the anisotropy of the exciton 1S wave function. (c) The exciton damping is due to phonon relaxation and is assumed to be uniform for a given exciton band. The experimentally observed RRS profiles are well fitted by the model calculations. From the parameters obtained by the fitting we conclude that the Bragg confined $(e_B{:}\mathrm{hh}_B)1S$ exciton is virtually two dimensional, while the $(e_B{:}\mathrm{lh}_B)1S$ and SL exciton $(e_1{:}\mathrm{hh}_1)1S$ are anisotropic to an intermediate degree between two and three dimensions. This work demonstrates that an analysis of the RRS profiles yields important information about the internal $(1S)$ exciton wave function and its relationship to the degree of exciton confinement.

ACKNOWLEDGMENTS

The research at the Technion was supported by the U.S.–Israel Binational Science Foundation (BSF), Jerusalem, Israel, and was done in the Barbara and Norman Seiden Center for Advanced Optoelectronics. M.Z. acknowledges the support of The Charles Clore 1979 Israel Foundation. E.L. acknowledges the support of the Center for Absorption in Science, Ministry of Immigrant Absorption, State of Israel.

---

[1] M. Zahler, I. Brener, G. Lenz, J. Salzman, and E. Cohen, Appl. Phys. Lett. **61**, 949 (1992).

[2] C. Sirtori, F. Capasso, J. Faist, D. L. Sivco, S.n. G. Chu, and A. Y. Cho, Appl. Phys. Lett. **61**, 898 (1992).

[3] F. Capasso, C. Sirtori, J. Faist, D. L. Sivico, S. Nee, G. Chu, and A. Y. Cho, Nature, **358**, 565 (1992).

[4] M. Zahler, E. Cohen, J. Salzman, E. Linder, and L. N. Pfeiffer, Phys. Rev. Lett. **71**, 420 (1993).

[5] M. Zahler, E. Cohen, J. Salzman, E. Linder, and L. N. Pfeiffer, J. Phys. (Paris) Colloq. **54**, C-343 (1993).

[6] M. Zahler, E. Cohen, J. Salzman, E. Linder, and L. N. Pfeiffer, Solid State Electron. **37**, 1195 (1994).

[7] C. Sirtori, J. Faist, F. Capasso, D. L. Sivco, and A. Y. Cho, Appl. Phys. Lett. **62**, 1931 (1993).

[8] B. Jusserand and M. Cardona, in *Light Scattering in Solids V*, edited by M. Cardona and G. Güntherodt (Springer, Berlin, 1989), Chap. 3, p. 133.

[9] W. Kauschke, A. K. Sood, M. Cardona, and K. Ploog, Phys.

Rev. B **36**, 1612 (1987).

[10] J. E. Zucker, A. Pinczuk, and D. S. Chemla, Phys. Rev. B **38**, 4287 (1988).

[11] D. A. Kleinman, R. C. Miller, and A. C. Gossard, Phys. Rev. B **35**, 664 (1987).

[12] A. J. Shields, C. Trallero-Giner, M. Cardona, H. T. Grahn, K. Ploog, V. A. Haisler, D. A. Tenne, N. T. Moshegov, and A. I. Tropov, Phys. Rev. B **46**, 6990 (1992).

[13] A. J. Shields, M. Cardona, R. Nötzel, and K. Ploog, Phys. Rev. B **46**, 10 490 (1992).

[14] S. Takagi, Acta Crystallogr. **15**, 1311 (1962).

[15] D. Taupin, Bull. Soc. Fr. Miner. Cristallogr. **87**, 469 (1964).

[16] R. M. Martin, Phys. Rev. B **4**, 3676 (1971).

[17] T. Takagahara, Phys. Rev. B **31**, 6552 (1985).

[18] M. Grundmann and D. Bimberg, Phys. Rev. B **38**, 13 486 (1988).

[19] G. Bastard, *Wave Mechanics Applied for Semiconductor Heterostrucures* (Les Editions de Physique, Les Ulis, 1989).

[20] B. K. Ridley, *Quantum Processes in Semiconductors* (Clarendon, Oxford, 1988).

[21] S. Datta, in *Modular Series on Solid State Devices, Vol. VIII–Quantum Phenomena,* edited by R. F. Pierret and G. W. Neudeck (Addison-Wesley, New York, 1989), p. 200.

[22] L. C. Andreani and A. Pasquarello, Phys. Rev. B **42**, 8928 (1991); L. C. Andreani, PhD. thesis, Scuola Normale Superiore, Pisa, 1989.